Parameterizations of Boundary Layer Mass Fluxes in High-Wind Conditions for Tropical Cyclone Simulations

XIAOMIN CHEN[a] AND FRANK D. MARKS[b]

[a] *Department of Atmospheric and Earth Science, University of Alabama in Huntsville, Huntsville, Alabama*
[b] *NOAA/OAR/Atlantic Oceanographic and Meteorological Laboratory, Miami, Florida*

(Manuscript received 5 May 2023, in final form 26 October 2023, accepted 6 November 2023)

ABSTRACT: Development of accurate planetary boundary layer (PBL) parameterizations in high-wind conditions is crucial for improving tropical cyclone (TC) forecasts. Given that eddy-diffusivity mass-flux (EDMF)-type PBL schemes are designed for nonhurricane boundary layers, this study examines the uncertainty of MF parameterizations in hurricane conditions by performing three-dimensional idealized simulations. Results show that the surface-driven MF plays a dominant role in the nonlocal turbulent fluxes and is comparable to the magnitude of downgradient momentum fluxes in the middle portion of TC boundary layers outside the radius of maximum wind (RMW); in contrast, the stratocumulus-top-driven MF is comparably negligible and exerts a marginal impact on TC simulations. To represent the impact of vertical wind shear on damping rising thermal plumes, a new approach of tapering surface-driven MF based on the surface stability parameter is proposed, aiming to retain the surface-driven MF only in unstable boundary layers. Compared to a traditional approach of MF tapering based on 10-m wind speeds, the new approach is physically more appealing as both shear and buoyancy forcings are considered and the width of the effective zone responds to diurnal variations of surface buoyancy forcing. Compared to the experiments retaining the original MF components, using either approach of MF tapering can lead to a stronger and more compact inner core due to enhanced boundary layer inflow outside the RMW; nevertheless, the radius of gale-force wind and inflow layer depth are only notably reduced using the new approach. Comparison to observations and further discussions on MF parameterizations in high-wind conditions are provided.

KEYWORDS: Boundary layer; Tropical cyclones; Hurricanes/typhoons; Mass fluxes/transport; Parameterization; Subgrid-scale processes

1. Introduction

Tropical cyclones (TC) are among the most devastating weather systems on the globe. While TC forecast skill has been steadily improved over the past decades thanks to the continuous development of numerical weather prediction (NWP) models, accurate forecasts of rapid intensification, structure evolution (e.g., secondary eyewall formation and replacement), and long-term track remain challenging (Fischer et al. 2019; Cangialosi et al. 2020). One important reason for these forecast challenges is the uncertainty of subgrid-scale parameterization schemes, as most of them are designed for non-TC applications. As such, TC modeling and forecasts have been frequently reported to be sensitive to the choice of planetary boundary layer (PBL) schemes (e.g., Braun and Tao 2000; Hill and Lackmann 2009; Nolan et al. 2009; Smith and Thomsen 2010; Bryan 2012; Zhang et al. 2015; Chen et al. 2021b; Chen and Bryan 2021). Reducing the uncertainty in PBL parameterizations in TC forecast models is crucial for further advancing model forecast skill. To achieve this goal and to overcome the limitation of scarce turbulence measurements under the extreme conditions of TC boundary layers, a modeling framework using large-eddy simulations (LES) was recently developed to evaluate and improve various types of PBL parameterizations in hurricane conditions (e.g., Chen et al. 2021a, 2022; Chen 2022).

Evaluation results in Chen (2022) indicated that the high-order, turbulence kinetic energy (TKE)-based PBL schemes [e.g., Mellor–Yamada–Nakanishi–Niino (MYNN)] are physically more complete in terms of turbulence generation and dissipation and have a better chance to succeed in modeling TC boundary layers. Nevertheless, incompatibility issues of surface-layer and PBL parameterizations and overestimated mixing length in hurricane conditions were identified in a TKE-based eddy-diffusivity mass-flux (hereafter EDMF-TKE) PBL scheme, which has been adopted in NOAA's next-generation hurricane forecast model, Hurricane Analysis and Forecast System (HAFS). A modified EDMF-TKE scheme was then proposed to address these issues (Chen et al. 2022). The two most important major changes in the modified scheme include 1) determining the values of coefficients in the eddy diffusivity and TKE dissipation term to match the surface-layer and PBL parameterizations and 2) reducing the maximum allow mixing length from 300 to 40 m based on LES results and observational values. Compared to the original EDMF-TKE, the modified EDMF-TKE scheme reduces the excessive vertical turbulent mixing in hurricane conditions, enhances the inflow strength, and further leads to improved intensity and structure forecasts in seasonal HAFS forecasts[1] (Chen et al. 2022, 2023).

Despite these encouraging results, the above assessment and improvement for EDMF-TKE are mostly applicable to the ED component or effective eddy viscosity, while the performance of the MF components, which represent nonlocal

Corresponding author: Xiaomin Chen, xc0011@uah.edu

[1] The modified EDMF-TKE scheme has been implemented into one of the two operational HAFS versions in 2023.

DOI: 10.1175/JAS-D-23-0086.1

turbulent mixing due to buoyant updrafts or downdrafts, remain unknown in hurricane conditions as they remain inactivated in the single-column modeling tests. This is in part attributable to the special setup of the modeling framework that anchors the thermodynamic profiles during the simulations (see details in Chen et al. 2021a). EDMF-type PBL schemes were developed to represent the turbulent processes in both dry and moist convective boundary layers (CBLs) (Siebesma and Teixeira 2000; Soares et al. 2004). Since high-order, EDMF-type PBL schemes are widely used in both global and regional NWP models for TC forecasts (e.g., Han and Bretherton 2019; Olson et al. 2019), understanding the representation of MF components in high-wind conditions is an important consideration for future PBL parameterization development. Moreover, accurate parameterizations of MF components in regional NWP models are also crucial to properly represent the boundary layer structure and processes in the scenario of TC–environmental vertical wind shear interactions (e.g., Gu et al. 2016; Ahern et al. 2021).

One unique feature intrinsic to high-wind or shear-driven boundary layers is that strong, local vertical wind shear can distort and damp buoyant plumes and thereby weaken the MF-related nonlocal turbulent mixing. Since shear-driven and buoyancy-driven boundary layers can be differentiated by stratification, a measure of the relative importance of buoyancy and shear production of TKE, investigating an optimal approach to control the MF contribution via stratification in shear-driven boundary layers is crucial. Both the MYNN-EDMF and modified EDMF-TKE schemes adopted a similar approach by linearly reducing surface-driven MF when the 10-m wind speed $V_{10} \geq 20$ m s^{-1} and turning off surface-driven MF when $V_{10} \geq 30$ m s^{-1} (henceforth referred to as *wind speed–based approach*). This approach essentially assumes that shear production of TKE alone controls the stratification. To overcome this limitation, this study proposes a different approach of MF "tapering" in shear-driven boundary layers based on the surface stability parameter (henceforth referred to as *stratification-based approach*). The main idea is to retain the MF components only in non-shear-driven boundary layers, as nonlocal turbulent mixing due to buoyant updrafts or downdrafts is intrinsic to buoyancy-driven boundary layers. The impact of these two approaches of MF tapering on TC intensity and structure will be examined by performing idealized three-dimensional simulations.

For simplicity, we will focus on the modified EDMF-TKE scheme at mesoscale grid spacings that are beyond boundary layer gray-zone[2] resolutions. The turbulent flux in EDMF-TKE is parameterized as (Han and Bretherton 2019)

$$\overline{w'\phi'} = -K_\phi\left(\frac{\partial\overline{\phi}}{\partial z}\right) + M_u(\phi_u - \overline{\phi})|_{\text{sfc}} + M_d(\phi_d - \overline{\phi})|_{\text{Sc}}, \quad (1)$$

where ϕ denotes one prognostic variable (e.g., potential temperature, winds, or TKE), the overbar denotes the horizontal average over a grid cell, K_ϕ denotes eddy diffusivities, M is mass flux, the subscripts u and d denote updraft and downdraft properties, respectively, and "sfc" and "Sc" denote surface-driven and stratocumulus-top-driven mass flux. Key questions to be addressed in this study include the following: 1) What is the impact of these MF components on the simulated TC intensity and structure? 2) Which MF component is more important in TC boundary layers? 3) What are the effects of the two approaches of MF tapering on TC modeling? Based on these findings, we will discuss an "optimal" way to reduce MF in hurricane conditions.

2. Experiment design and model setup

Version 20 of Cloud Model 1 (CM1; Bryan and Fritsch 2002) is used in this study for idealized three-dimensional TC simulations. Following Chen and Bryan (2021), the model is initialized with an axisymmetric TC vortex in a quiescent environment on an f plane with a Coriolis parameter of 5×10^{-5} s^{-1}. The radial profile of the tangential wind of the initial vortex follows a modified Rankine vortex, where the radius of the maximum wind (RMW) is set to 80 km and the maximum tangential wind V_m is set to 10 m s^{-1} near the surface. The value of V_m decreases linearly to zero from the surface to 12-km height, the top level of the initial vortex. One large model domain is used, with a horizontal grid spacing of 3 km within the central 600 km × 600 km area, outside of which the horizontal grid spacing is gradually stretched to 15 km. The model domain follows the motion of simulated TCs. In the vertical direction there are 59 model levels, which are stretched in the vertical so that there are more model levels in the boundary layer. The height of the bottom model level is 50 m. The output frequency is every 1 h. The selected model physics schemes are consistent with Chen and Bryan (2021), except for the PBL scheme. The modified EDMF-TKE PBL scheme is used in this study given its better performance in hurricane conditions than the original EDMF-TKE scheme (Chen et al. 2022, 2023).

To examine the impact of different MF components as well as the two approaches of MF tapering in high-wind conditions on TC modeling, different sets of experiments using the modified EDMF-TKE scheme but varying the settings for the MF components are performed (see details in Table 1). As the proposed stratification-based approach of MF tapering is to retain MF only in non-shear-driven boundary layers, the last three experiments in Table 1 are performed to identify an appropriate threshold of surface stability parameter ζ that can differentiate TC and non-TC boundary layers. $\zeta = z/L$, where z is the height of the lowest model level and L is Monin–Obukhov length. ζ essentially reflects the ratio of buoyancy production of turbulence to shear production of turbulence. The boundary layer is typically considered "very unstable" when $\zeta < -0.5$ (e.g., Han et al. 2016). Since TC boundary layers are nearly neutral (e.g., Foster 2013; Chen 2022), we also test the "weakly unstable" or nearly neutral conditions ($-0.5 < \zeta < 0$) in experiments MF–0.1 and MF–0.05. Each experiment is initialized with a moist tropical sounding (Dunion 2011), and the default sea surface temperature (SST) is set to 29°C. Since surface-driven MF is dependent on the surface

[2] In the boundary layer gray zone, horizontal grid spacings are comparable or smaller than the diagnosed boundary layer height such that turbulence is partially resolved by model grids (see an example in Chen et al. 2021b).

TABLE 1. Experiments based on the modified EDMF-TKE scheme and the related descriptions.

Experiment	Descriptions of MF parameterizations
CTL	Untapered MF components
NOMF	Set $M_u = M_d = 0$
NOSFC	Set $M_u = 0$
NOSC	Set $M_d = 0$
TaperMF	M_u and M_d are linearly tapered when $V_{10} \geq 20$ m s^{-1} and turned off when $V_{10} \geq 30$ m s^{-1} (Chen et al. 2022, 2023)
MF–0.5	Activate M_u only where surface stability parameter $\zeta < -0.5$
MF–0.1	Activate M_u only where surface stability parameter $\zeta < -0.1$
MF–0.05	Activate M_u only where surface stability parameter $\zeta < -0.05$

heat flux or buoyancy, we performed additional sets of experiments by increasing the SST to 30° and 31°C. To note, other sets of sensitivity experiments by varying V_m and decay rate of the tangential wind outside the RMW are performed, which are consistent with the findings from the above simulations and therefore not shown.

3. Effects of MF components on TC intensity and structural changes

This section addresses two key questions raised at the end of the introduction: 1) what is the impact of parameterized MF on TC simulations and 2) which MF component is more important for TC modeling? We examined four experiments, which turn on both M_u and M_d (CTL), turn off both M_u and M_d (NOMF), turn off M_u only (NOSFC), and turn off M_d only (NOSC), respectively. Figure 1 shows the simulated TC intensity and structure from these experiments. Comparison of the CTL and NOMF experiments (black and red lines) indicates that turning off both MF components in EDMF-TKE leads to stronger TC intensity, in terms of 10-m maximum azimuthal-mean tangential wind, and smaller RMW during the majority of simulation periods (Figs. 1a,b). Of note, the evolution of minimum sea level pressure from the four experiments yields consistent results as in Fig. 1a (not shown). Importantly, the TC outer-core size in terms of gale-force wind radius (henceforth R17) shrinks 10%–20% in NOMF compared to CTL. Additional NOSFC and NOSC experiments (blue and green lines in Fig. 1) indicate that differences between CTL and NOMF are mostly attributable to the surface-driven MF, as NOSFC produces comparable maximum intensity, RMW, and R17 with NOMF while NOSC behaves similarly with CTL. Of note, this finding is robust for various SSTs and different initial vortices (not shown). Thus, surface-driven MF dominates the impact of MF on TC intensity and structural changes, while stratocumulus-top-driven MF only plays a minor role.

To understand the impact of the two MF components, Fig. 2 shows the radius–height structure of the azimuthal-mean MF and K_m-related momentum fluxes averaged over

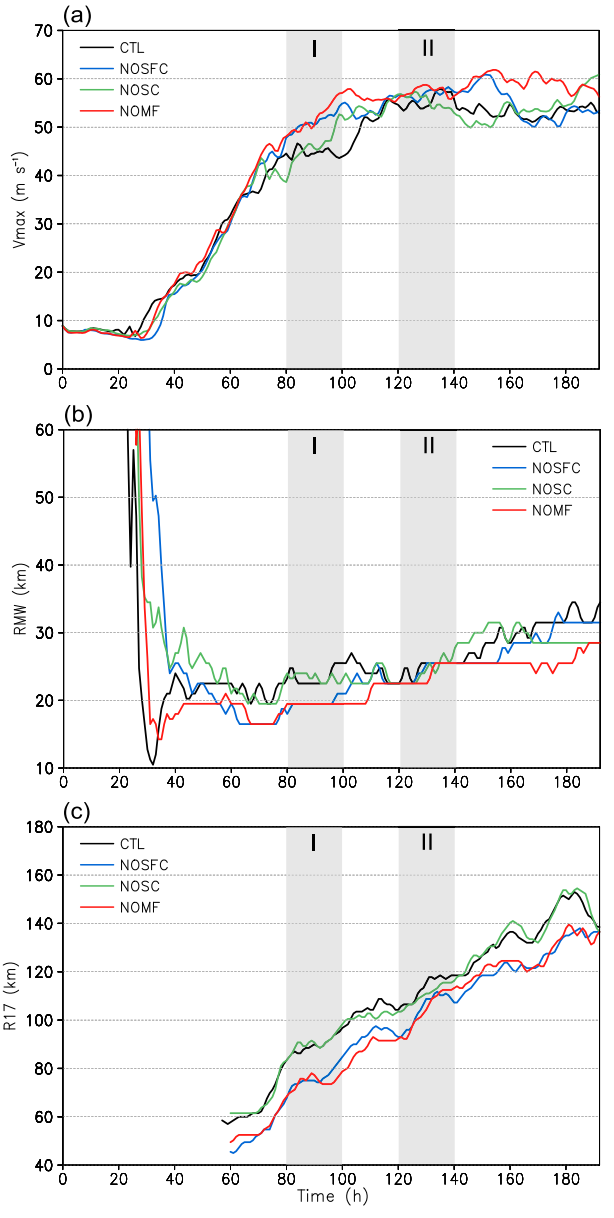

FIG. 1. Evolution of (a) 10-m maximum azimuthal tangential wind (m s^{-1}), (b) RMW (km), and (c) R17 (km) from CTL (black), NOMF (red), NOSFC (blue), and NOSC (green) experiments. The gray-shaded boxes denote two analysis periods in this study. R17 in (c) is shown after the simulated TC reaches hurricane intensity.

two periods, i.e., t = 80–100 h (period 1) and 120–140 h (period 2), from the CTL experiment. The simulated TC vortex in CTL is in a quasi-steady state during both periods. Over period 1, the maximum 10-m azimuthal-mean tangential wind (hereafter VMAX) in CTL is 45 m s^{-1}. The surface-driven MF M_u is activated at all radii. Radially, M_u is maximized outside the RMW. The dip in the magnitude of M_u at the RMW is attributable to the high winds that lead to a very small surface stability parameter ζ (i.e., nearly neutral,

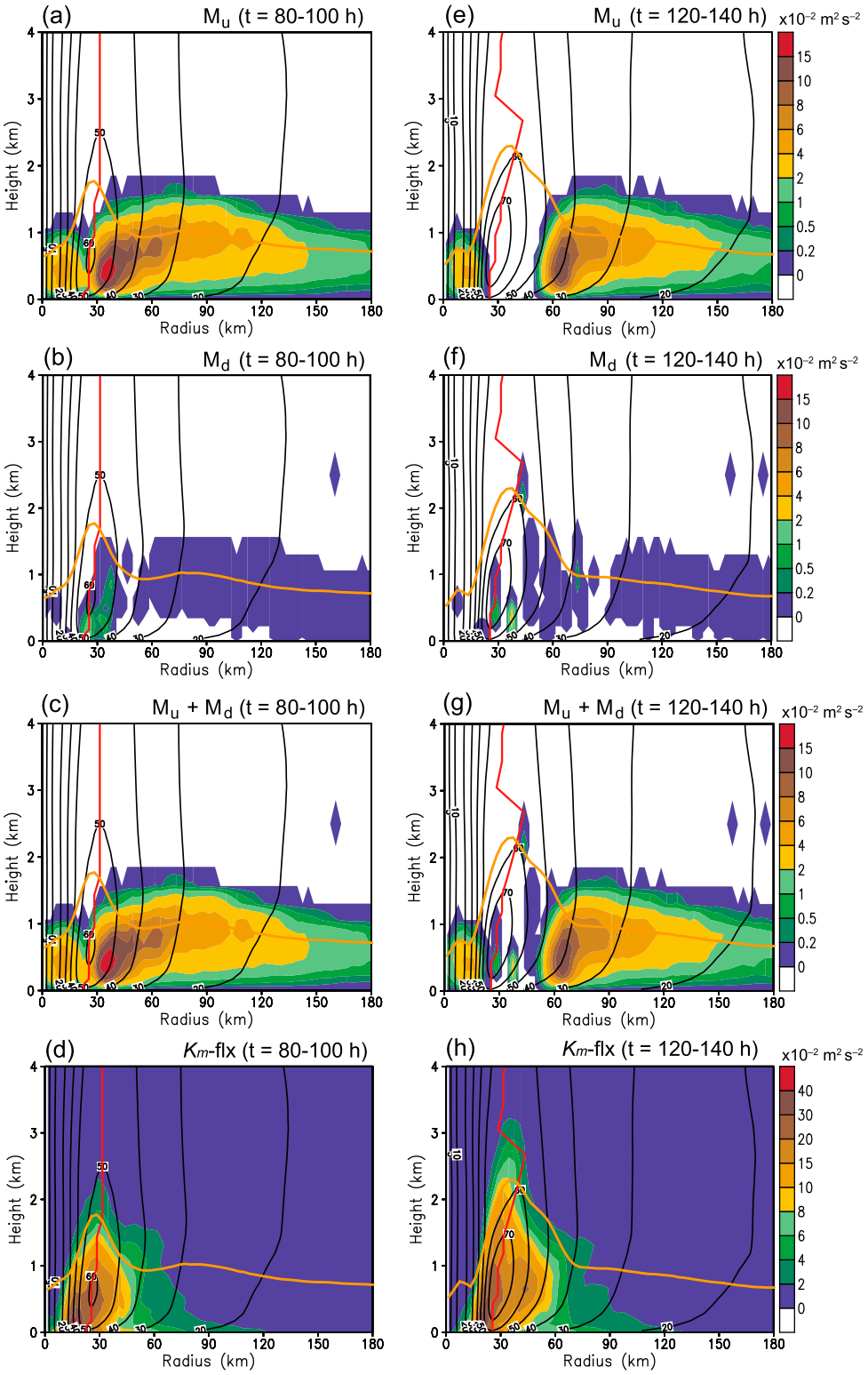

FIG. 2. Radius–height distribution of azimuthally averaged MF and K_m-related downgradient momentum fluxes (shading; m^{-2} s^{-2}) and tangential wind (black contours of 20, 30, 40, 50, and 60 m s^{-1}) during the periods of t = (left) 80–100 and (right) 120–140 h from the CTL experiment. (a),(e) M_u, (b),(f) M_d, (c),(g) M_u + M_d, and (d),(h) K_m-related downgradient momentum fluxes. In each panel, the orange line denotes the diagnosed PBL height and the red line denotes the RMW. Of note, the shading scales in (d) and (h) are different from other panels.

$\zeta > -0.02$) such that M_u is deactivated (as prescribed in the EDMF-TKE code). Vertically, M_u is maximized in the 500–800 m layer, approximately the central part of the PBL MF column at each radius. This is attributable to the setting of the smallest entrainment rate in the middle of the PBL code, which is consistent with the documented maximum vertical velocity variance in the middle of buoyancy-driven boundary layers (Moeng and Sullivan 1994). Comparison of Figs. 2a and 2b indicates that the magnitude of stratocumulus-top-driven M_d is generally negligible compared to M_u, with the only exception occurring near the RMW. This finding accounts for the minor impact of M_d on the TC intensity and RMW (Figs. 1a,b). Figures 2c and 2d further compare the magnitude of the total MF and K_m-related momentum fluxes in the TC circulations. A quick glance indicates that M_u dominates the boundary layer vertical mixing outside the RMW. K_m-related momentum fluxes are mostly concentrated within the 3 × RMW, with the maximum value residing inside the RMW. Over period 2, the TC circulation is further enhanced along with the K_m-related downgradient turbulent mixing (Fig. 2h). M_u becomes deactivated within r = 30–45 km, where boundary layer conditions (in terms of ζ) become nearly neutral under higher wind speeds. Nevertheless, the findings over period 1 are still applicable to period 2 (Figs. 2e–h).

To further quantify the relative importance between MF and K_m-related momentum fluxes outside the RMW, Fig. 3 shows their vertical profiles averaged within the annulus of r = 30–120 km over period 1 (solid lines) and within the annulus of r = 45–120 km over period 2 (dashed lines). Since M_u is deactivated within r = 30–45 km over period 2 (Fig. 2e), a different annulus is used for period 2. Results indicate that M_u dominates the vertical momentum flux in the middle–upper boundary layer (400–1200 m), and the maximum value of M_u is ~60% greater than that of the K_m-related momentum flux. Consistent with earlier discussions, the magnitude of M_d is negligible compared to both M_u and K_m-related momentum flux. Similar findings can be found over period 2 despite the increase of the K_m-related momentum flux (Fig. 2). The above analysis demonstrates the dominant role of M_u in the boundary layer turbulent mixing in the mid–upper portion of the boundary layer outside the RMW.

Figure 4 shows the mean boundary layer inflow structure over period 1 from the CTL, NOSC, NOSFC, and NOMF experiments. Comparison of the CTL and NOSC experiments (Figs. 4a,b) indicates very similar boundary layer structures, including the maximum inflow strength outside the RMW, diagnosed boundary layer height (orange line), and inflow layer depth (i.e., the level of $V_r = -1$ m s^{-1}, blue dashed line). Differences in the boundary layer inflow between CTL and NOSC (Fig. 5a) indicate that NOSC has slightly stronger inflow immediately outside the RMW, where the M_d is maximized in CTL and turned off in NOSC (Fig. 2b), suggesting the reduced vertical mixing near the RMW slightly accelerates the boundary layer inflow therein by ~2 m s^{-1}. This explains the stronger TC intensity during the last few hours of period 1 in NOSC (Fig. 1a), but its overall impact on the TC intensity and structure is insignificant. Figure 5d further shows that the exclusion of M_d in NOSC leads to a more humid lower troposphere

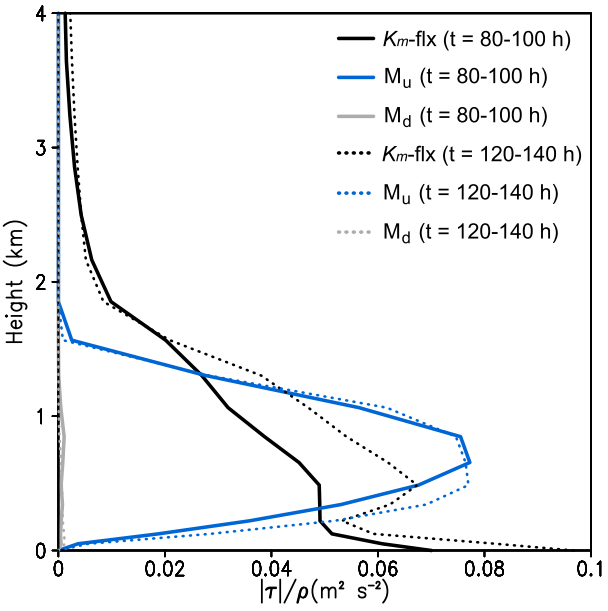

FIG. 3. Vertical profiles of K_m-related momentum fluxes (black), M_u (blue), and M_d (gray) averaged within the annulus of r = 30–120 km over t = 80–100 h (solid lines) and within the annulus of r = 45–120 km over t = 120–140 h (dashed lines).

(<4 km) over period 1, especially at large radii (r = 90–180 km). We suspect the reduction of stratocumulus-top-driven downdraft mixing alleviates dry air intrusion, which further encourages stronger surface-driven MF as the lateral entrainment weakens. Comparison of CTL and NOSFC experiments (see Figs. 4a,c) indicates a strikingly different boundary layer structure: in NOSFC the inflow layer depth is ~500 m shallower, the maximum boundary layer inflow is ~5 m s^{-1} stronger, and the RMW averaged below 1-km height is ~16% smaller.

To quantify these differences, Fig. 5b shows that the maximum difference in the inflow strength between CTL and NOSFC is >8 m s^{-1} located near the RMW. Differences in the specific humidity (Fig. 5e) further show that the exclusion of M_u leads to a moister near-surface layer underneath a drier layer in NOSFC. This can be interpreted as more water vapor being able to stay near the surface in the absence of surface-driven buoyant updrafts. Comparison of NOSFC and NOMF (Figs. 4c,d), together with the related difference plots relative to CTL (Figs. 5b,c,e,f), indicates a similar boundary layer structure, confirming the earlier findings regarding the dominant role of M_u in the two MF components. The stronger boundary layer inflow in NOSFC (or NOMF) can contribute to the more efficient radial advection of large absolute angular momentum from large radii toward the inner core, which accounts for the stronger simulated TC intensity and smaller inner- and outer-core sizes in NOSFC (or NOMF) than in CTL.

4. Two approaches to taper off surface-driven mass flux in high-wind conditions

Since surface-driven MF (M_u) dominates the two MF components in the EDMF-TKE, this section focuses on the

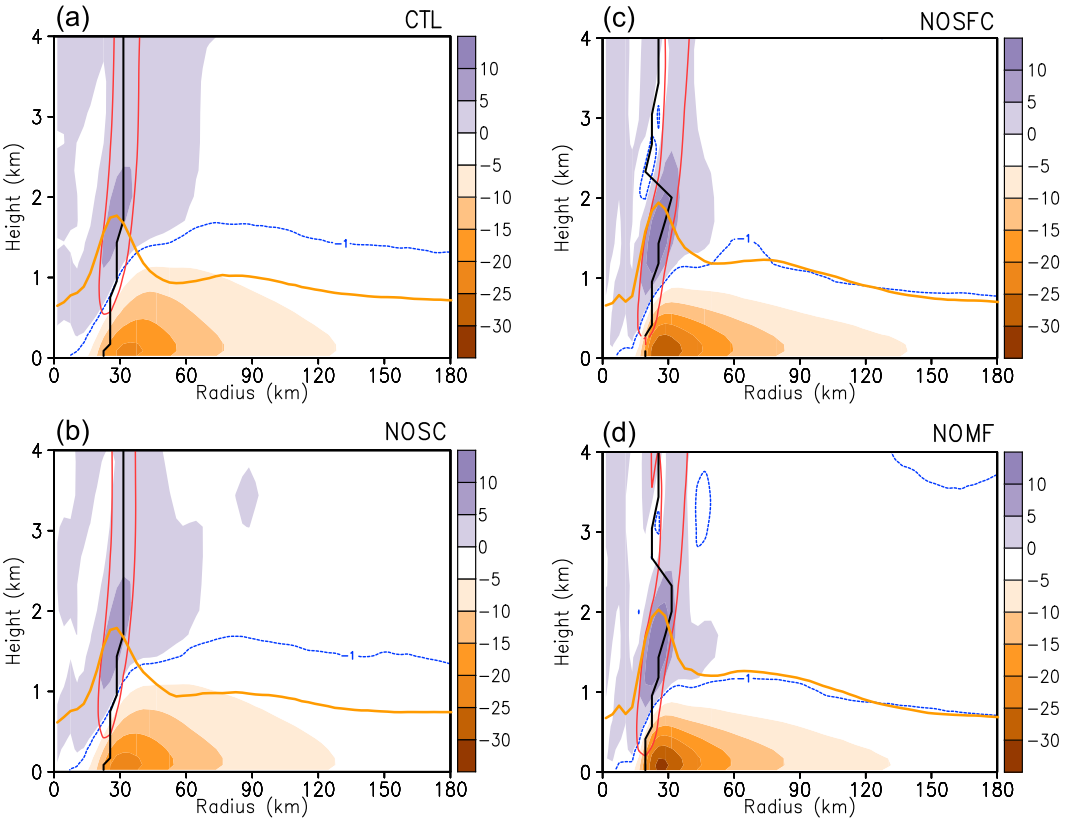

FIG. 4. Radial–height plot of azimuthally averaged radial velocity (shading; m s^{-1}) over t = 80–100 h for (a) CTL, (b) NOSC, (c) NOSFC, and (d) NOMF experiments. The red contour denotes w = 1 m s^{-1}, the black line represents the mean RMW, the orange line denotes the mean diagnosed PBL height h, and the dashed blue line denotes inflow layer depth ($V_r = -1$ m s^{-1}).

parameterizations of M_u in high-wind conditions. To represent the effects of strong vertical wind shear in distorting and damping rising thermal plumes, the modified EDMF-TKE scheme in Chen et al. (2022) uses a wind speed–based approach to reduce MF in high-wind conditions, following the MYNN code from WRF V4.2. This section investigates a stratification-based approach that only retains MF in non-shear-driven boundary layers based on the surface stability parameter ζ, as discussed in section 2, and compares the performance of these two approaches. Driven by surface heat fluxes, the strength of M_u is closely related to SST. To identify an appropriate threshold of ζ that can separate shear-driven and non-shear-driven boundary layers effectively under different scenarios, two additional sensitivity tests based on the CTL experiment but with warmer SSTs (30° and 31°C) are performed, referred to as CTL-30C and CTL-31C, respectively.

Figures 6a–c show the azimuthal-mean ζ and V_{10} from the CTL experiments using different SSTs, and Figs. 6d–f highlight the effective zone where M_u is tapered or turned off using the wind speed–based approach (blue shading) as well as the stratification-based approach using different thresholds of ζ (red shading). The blue shading can be roughly considered as the overlapping region of the two approaches. As documented earlier, the wind speed–based approach becomes effective when $V_{10} \geq 20$ m s^{-1}, which occurs approximately 10 h earlier in CTL-30C and CTL-31C experiments than in CTL, as vortex spinup is faster in the former two experiments. The innermost radius of the blue shading outside the RMW[3] in Figs. 6d–f denotes the contour of $\zeta = -0.02$ (see Figs. 6a–c), the threshold to trigger M_u in the EDMF-TKE code. The effective zone of $\zeta > -0.05$ is comparable to that of the wind speed–based approach, except that it exhibits a more notable diurnal oscillation and has a larger width during nocturnal times under relatively lower SSTs (Figs. 6a,b). When $\zeta > -0.1$ and $\zeta > -0.5$, the effective zone of the stratification-based approach extends to the radii where $V_{10} \in [10, 20]$ m s^{-1} and $V_{10} < 10$ m s^{-1}, respectively (Figs. 6d–f). Clearly, the stratification-based approach with $\zeta > -0.5$ has the widest effective zone and becomes activated earliest among all different settings of the first and second approaches. One interesting phenomenon is that when $\zeta > -0.5$, the MF tapering is activated during the initial spinup hours ($t < 20$ h) near the RMW in the CTL and CTL-30C experiments. Overall, the stratification-based approach with different ζ thresholds can effectively

[3] Blue shadings also exist inside the RMW but cover a relatively narrow annulus.

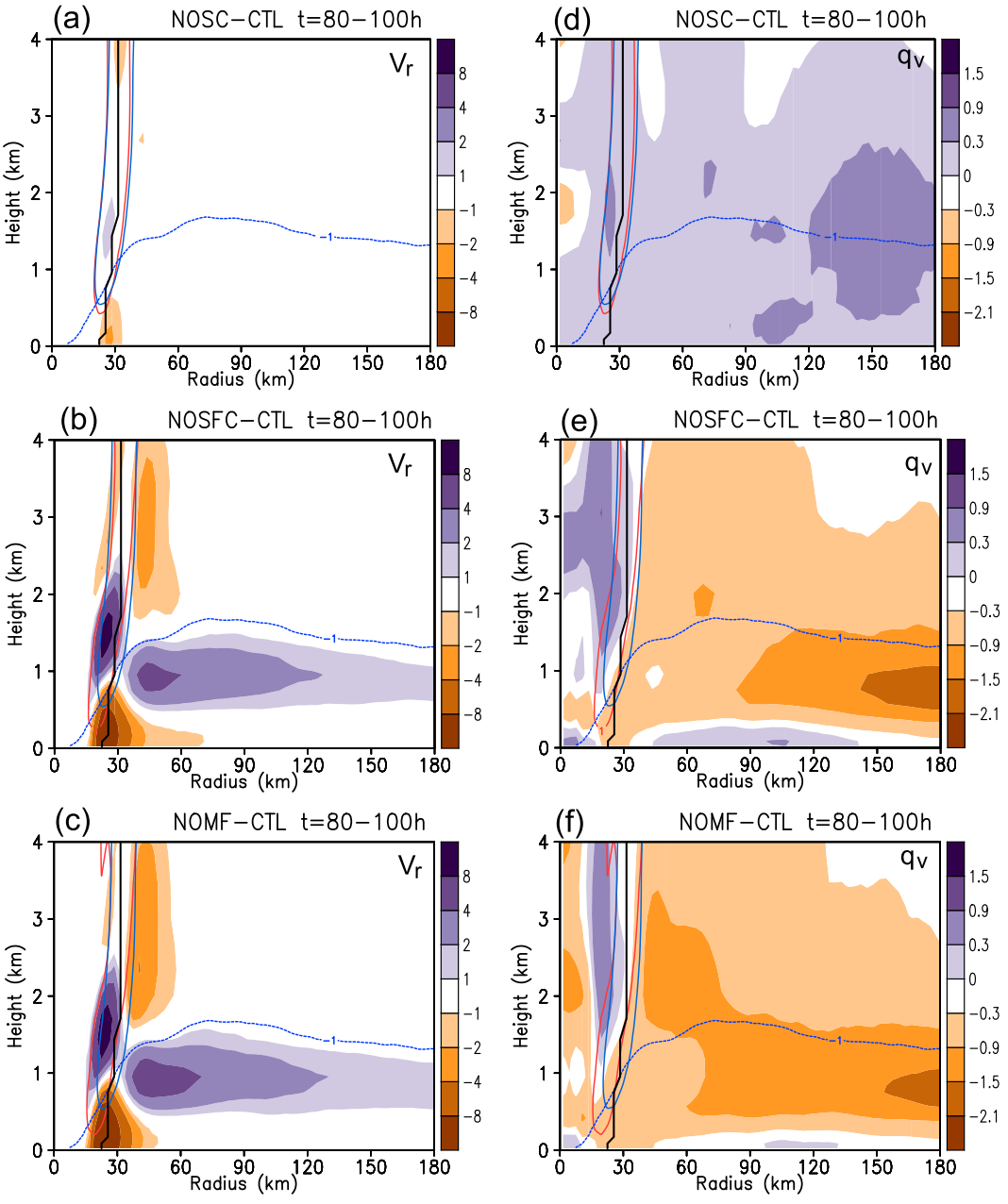

FIG. 5. (a)–(c) Differences in the radius–height structure of azimuthal-mean radial winds (shading; m s^{-1}) between sensitivity tests and CTL experiment: (a) NOSC − –CTL, (b) NOSFC − –CTL, and (c) NOMF − –CTL. The red (blue) contour denotes $w = 1$ m s^{-1} in the sensitivity (CTL) experiment. The black line and blue dashed line represent the mean RMW and $V_r = -1$ m s^{-1} in CTL, respectively. (d)–(f) As in (a)–(c), but the shading denotes specific humidity (g kg^{-1}).

identify high-wind regions and respond to the diurnal oscillation of near-surface buoyancy forcing under various SSTs, which shows promise for future applications.

Figure 7 compares the evolution of VMAX, RMW, and R17 from CTL, MF–0.05, MF–0.1, MF–0.5, and TaperMF experiments under different SSTs. The TaperMF, MF–0.05, and MF–0.1 experiments produce similarly stronger VMAX than CTL under different SSTs (Figs. 7a,d,g). In comparison, TCs in the MF–0.5 experiment (blue line) undergo a slightly longer preconditioning period before RI onset and have weaker maximum intensity than the TaperMF, MF–0.05, and MF–0.1 experiments under SST = 29° and 30°C. The difference in the preconditioning period disappears under SST = 31°C, suggesting the strong surface-driven MF under very warm SST helps spin up the TC vortex, likely through moistening the boundary layer that facilitates the eyewall cloud formation. In terms of RMW, the two approaches

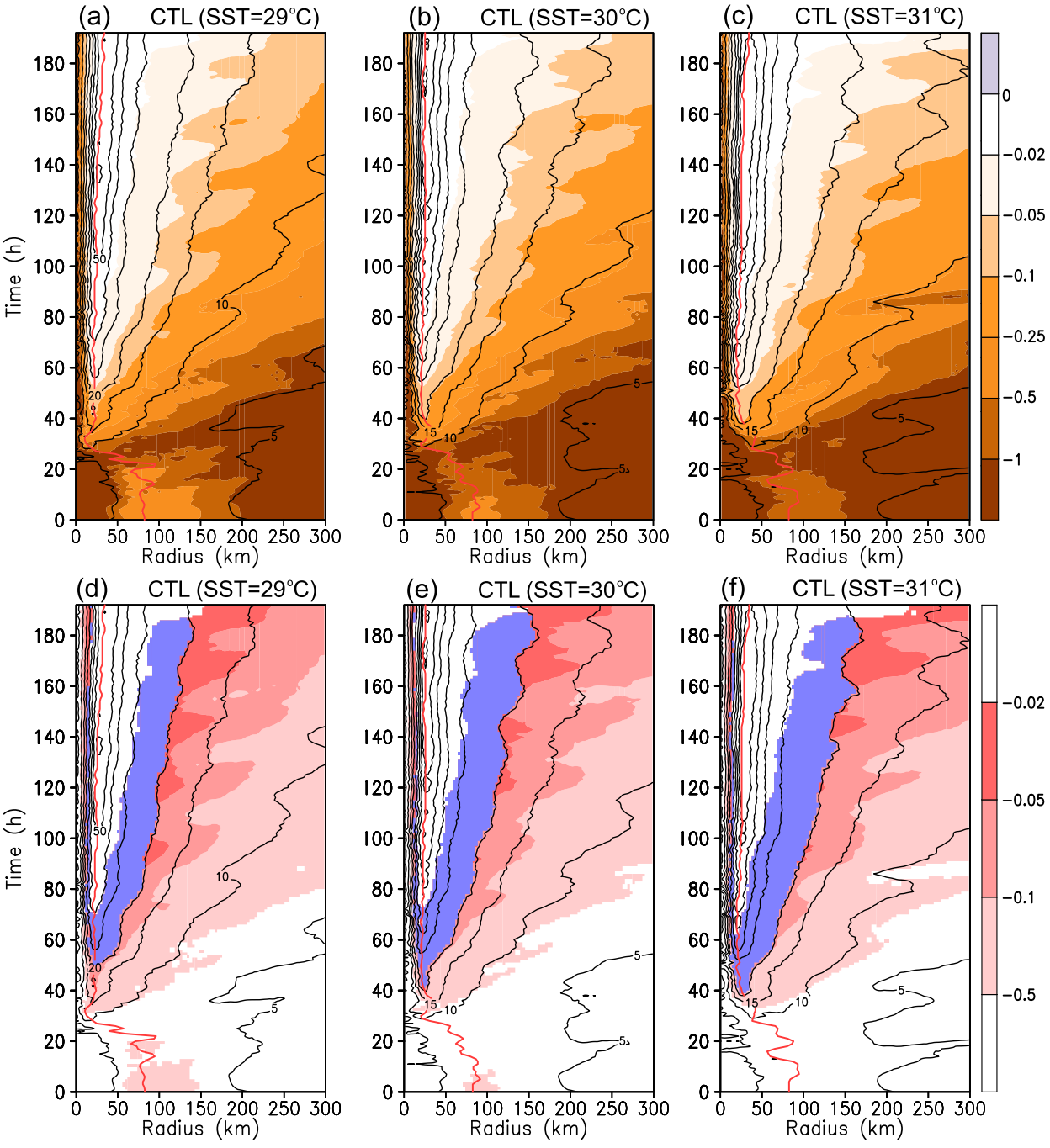

FIG. 6. (a)–(c) Hovmöller diagram of azimuthal-mean surface stability parameter ζ (shading) and V_{10} (contoured at 10, 15, 20, 30, 40, 50, and 60 m s^{-1}) from the CTL experiments with SST = 29°, 30°, and 31°C, respectively. (d)–(f) As in (a)–(c), but showing the region where two approaches of M_u tapering are applicable. The blue shading is where the azimuthal-mean V_{10} is greater than 20 m s^{-1} and $\zeta < -0.02$. Red shadings demonstrate the region where M_u is turned off with different ζ thresholds (e.g., −0.05, −0.1, −0.5). The red line in each panel represents the RMW from each experiment.

produce similarly more compact RMW than the CTL experiment; the only exception is the MF–0.5 experiment over t = 110–160 h under SST = 29°C (Figs. 7b,e,h).

The largest difference between the five experiments lies in R17 (Figs. 7c,f,i). Compared to CTL, the R17 in TaperMF is nearly unaffected under different SSTs, which is consistent with its effective zone being confined radially inward of R17 (see Fig. 6) and also agrees with the results of idealized simulations in Chen et al. (2022). The R17 evolution in MF–0.05 resembles that in TaperMF, although the amplitude of diurnal

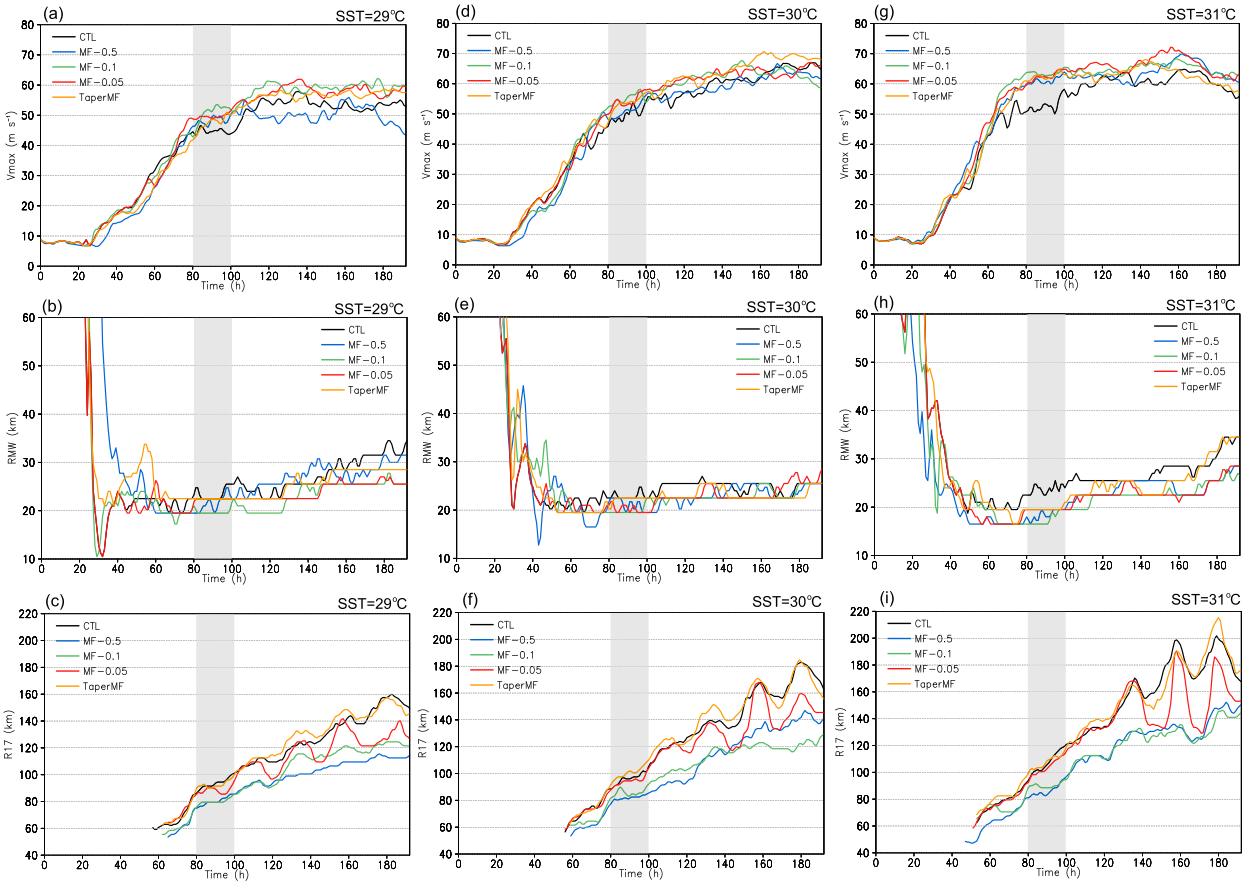

FIG. 7. Evolution of (a) 10-m maximum azimuthal tangential wind (m s^{-1}), (b) RMW (km), and (c) R17 (km) from CTL (black), MF–0.5 (blue), MF–0.1 (green), MF–0.05 (red), and TaperMF (orange) experiments with SST = 29°C. (d)–(f),(g)–(i) As in (a)–(c), but with SST = 30° and 31°C, respectively. The gray-shaded box in each panel denotes the analysis period. R17 is shown after the simulated TC reaches hurricane intensity.

variations of R17 in MF–0.05 is much greater than in TaperMF, which is closely related to the diurnal variation of their effective zone as shown in Fig. 6. The R17 in MF–0.5 and MF–0.1 is consistently smaller than that in MF–0.05, TaperMF, and CTL. Interestingly, the R17 in CTL and TaperMF grows much faster after t = 100 h than in MF–0.5 and MF–0.1, leading to a maximum difference of 50–60 km after t = 150 h under different SSTs.

Differences in the intensity and structure using the two approaches of MF tapering are closely related to the boundary layer structure. One insightful metric to indicate inflow strength is surface inflow angle, defined as $\tan^{-1}(V_{R10}/V_{T10})$, where V_{R10} and V_{T10} are the radial and tangential velocities at 10-m height, respectively. Figure 8 compares the radial profile of surface inflow angle from different experiments under various SSTs over t = 80–100 h. During this period, the simulated TCs reach a quasi-steady state and have comparable VMAX and RMW. The inflow is accelerated in all MF tapering experiments compared to the CTL experiment, with the radial extent of acceleration being different between MF tapering experiments. The magnitude of inflow angle is increased by 7°–10° within 1–5 × RMW in the MF–0.5 and MF–0.1 experiments; while the increase of inflow angle is mostly confined within the 1–3 × RMW in MF–0.05 and TaperMF experiments. The acceleration of inflow is typically more notable in MF–0.05 than in TaperMF; one exception occurs under SST = 31°C and the acceleration of inflow in these two experiments becomes nearly identical, which is consistent with Fig. 6f in that the effective zone of MF tapering becomes nearly overlapped prior to t = 140 h under very warm SST. Figure 8 also provides the observed 10-m inflow angle from a dropsonde composite of category 1–5 hurricanes (Zhang and Uhlhorn 2012) as a reference. Despite the differences in VMAX of CTL TCs under different SSTs, the surface inflow angle in CTL is very close to the dropsonde composites and surprisingly stays nearly invariant. We suspect the nearly invariant inflow angle under different TC intensity produced by the original EDMF-TKE scheme is unrealistic, which is likely an outcome of excessive turbulent mixing in the core region due to the inclusion of the original MF parameterizations. We call for more future efforts to stratify the observed inflow angle by TC intensity to provide better insights for the verification. In comparison, the inflow angle is typically greater in MF-tapering experiments, and the increase in inflow angle amplifies with SSTs as the VMAX of simulated TCs is greater as SST increases.

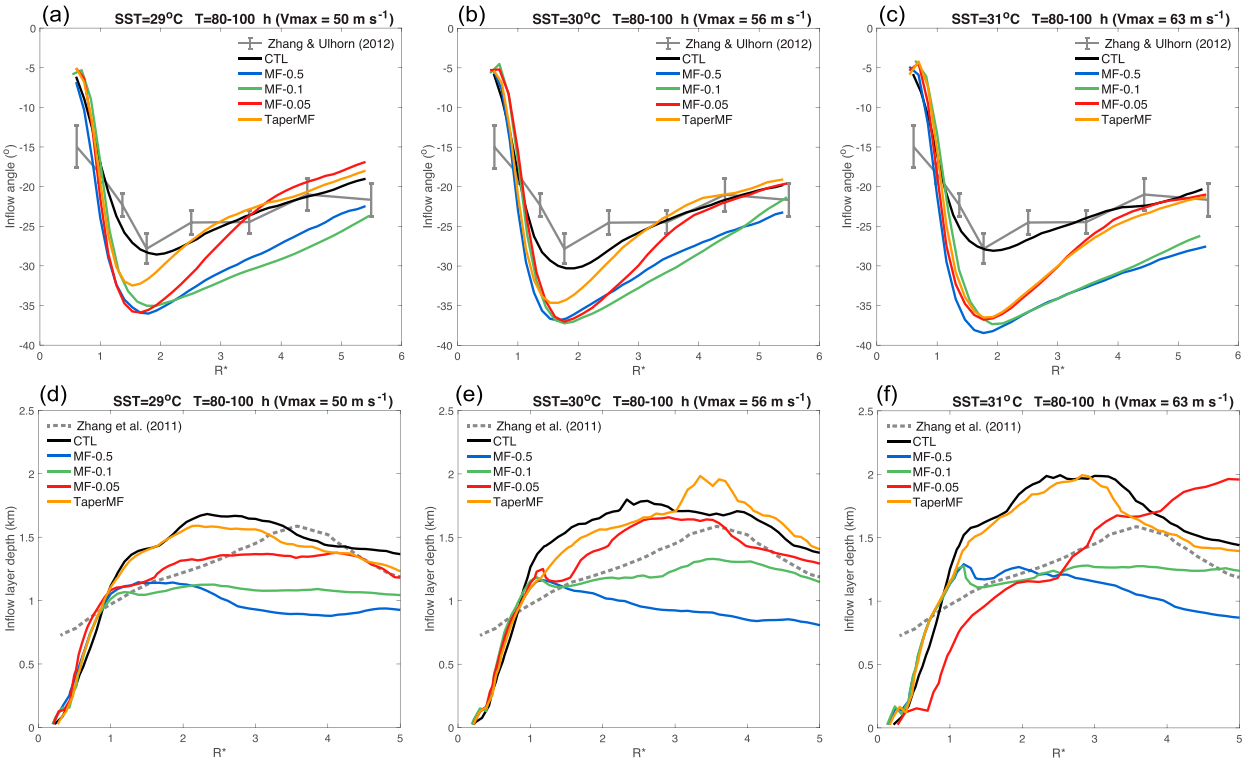

FIG. 8. (a)–(c) Composite 10-m radial profile of inflow angle as a function of normalized radius R^* ($=R$/RMW) from CTL (black), MF–0.5 (blue), MF–0.1 (green), MF–0.05 (red), and TaperMF (orange) experiments under (a) SST = 29°C, (b) SST = 30°C, and (c) SST = 31°C. The composite period is shown in Fig. 7. The 10-m radial profile of inflow angle from a dropsonde composite of category-1–5 hurricanes (Zhang and Uhlhorn 2012) is shown for a reference (gray); the gray bar denotes the 95% confidence intervals. The maximum intensity of simulated TCs averaged over the composite period is shown at the top of each panel. (d)–(f) As in (a)–(c), but for the modeled inflow layer depth (indicated by $V_r = -1$ m s^{-1}) against the observations from Zhang et al. (2011) (gray dashed line). Of note, the range of abscissa in (d)–(f) is slightly different from that in (a)–(c).

Figures 8d–f compare the radial profile of inflow layer depth, indicated by $V_r = -1$ m s^{-1}, from these simulations and in situ observations[4] (Zhang et al. 2011). The same composite period for model results is chosen as in Figs. 8a–c. The observed inflow layer depth is extracted from the composite radial winds based on 794 dropsonde released in category 1–5 hurricanes (see Fig. 5b in Zhang et al. 2011). The main difference in the inflow layer depth between observation, CTL, and TaperMF lies within 1–3 × RMW. The inflow layer depth in CTL and TaperMF is generally ≥500 m deeper than observations, and the differences increase as the TC intensity increases with SST. In contrast, MF–0.5 and MF–0.1 produce shallower inflow within 2–5 × RMW than observations. One interesting phenomenon is that the inflow layer depth within 1–4 × RMW in MF–0.05 is similar to observational values to within 300 m. While this result is seemingly promising, one needs to be aware that the sampling size of dropsonde at each radial bin outside the RMW is only 20–40 (cf. Fig. 3 in Zhang et al. 2011). Once again, this comparison emphasizes the need for collecting additional observations through dropsondes and other profiling systems in future studies.

Given that Fig. 8 is based on the normalized radius R^*, examining the modeled radial wind structure along actual radii can yield additional insights into the impact of MF control choices, especially for those MF tapering experiments where only the inner-core (not the outer-core) size is affected (e.g., TaperMF). Figure 9 presents an example under SST = 29°C, showing the differences in the radius–height structure of azimuthal-mean radial wind averaged over the same period. Differences in the inflow strength above the surface layer in Fig. 9 supplement the comparison of the near-surface inflow angle in Figs. 8a–c. Compared to CTL, the inflow depth (gray dashed lines in Figs. 9a–c) is consistently lowered outside the RMW using the stratification-based approach of MF tapering, with maximum reduction of ~800 m in MF–0.5, ~600 m in MF–0.1, and ~300 m in MF–0.05. This finding is consistent with Figs. 8d–f. Meanwhile, the inflow at the lower boundary layer in these three experiments is stronger, especially near the RMW, and the zone of enhanced inflow extends to larger radii in MF–0.5 and MF–0.1 than in MF–0.05. In contrast, the wind speed–based approach of MF (i.e., TaperMF) exerts a

[4] Zhang et al. (2011) defined inflow layer depth as the level where the radial velocity is 10% of the peak inflow. For a fair comparison between model results and observations, we recalculated the observed inflow layer depth as the level where $V_r = -1$ m s^{-1}.

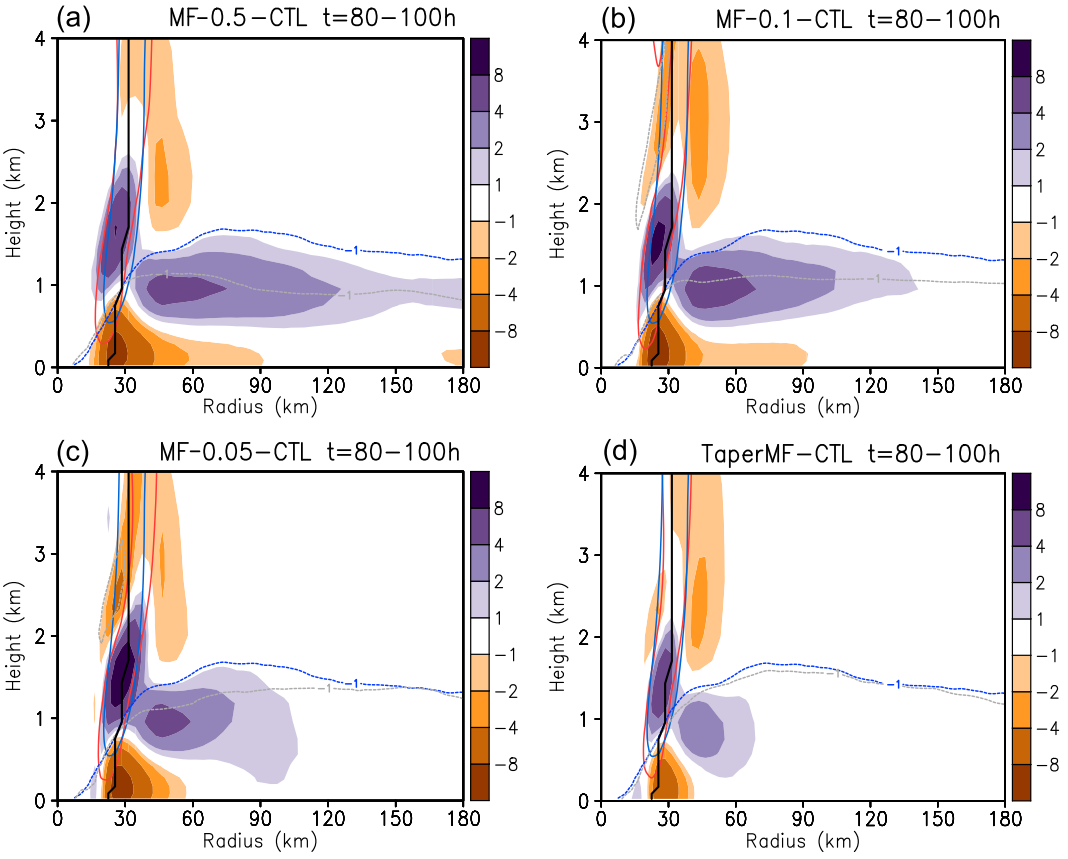

FIG. 9. Difference in the radial–height distribution of azimuthal-mean radial wind (shading; m s^{-1}) averaged over t = 80–100 h between the CTL and other experiments with SST = 29°C, showing (a) MF–0.5 − CTL, (b) MF–0.1 − CTL, (c) MF–0.05 − CTL, and (d) TaperMF − CTL. In each panel, the blue dashed line and blue contour denote $V_r = -1$ m s^{-1} and $w = 1$ m s^{-1} in CTL, respectively; the gray dashed line and red contour denote $V_r = -1$ m s^{-1} and $w = 1$ m s^{-1} from the other comparison experiment. The black line denotes the RMW in CTL. Orange or brown shading below 1-km height means that the MF control choice produces stronger inflow than CTL.

marginal effect on the inflow depth with the effective region being confined near the RMW (Fig. 9d). Additionally, the acceleration of inflow near the RMW in TaperMF is less notable than the experiments using the stratification-based approach of MF tapering (Fig. 9), which is consistent with the comparison of surface inflow angle (Fig. 8a). These results demonstrate that both the inflow depth and strength above the surface is altered by MF tapering.

In short, the above findings demonstrate that the stratification-based approach of MF tapering impacts not only the inflow strength but also the inflow depth, while the wind speed–based approach of MF tapering mostly affects the inflow strength near the RMW. The enhanced boundary layer inflow within the inner core supported the smaller RMW and stronger VMAX in these MF tapering experiments than in CTL, as stronger boundary layer inflow can advect large absolute angular momentum (AAM) from larger radii inward toward the TC center (Smith and Montgomery 2015; Chen and Bryan 2021).

Figures 9a and 9b also indicate that the inflow strength near R17 in these experiments (r = 80–90 km over t = 80–100 h; see Fig. 7c) is 1–2 m s^{-1} stronger in MF–0.5 and MF–0.1 than in CTL. Stronger inflow will advect large AAM from larger radii inward, which typically contributes to the expansion of R17 with the assumption that the loss of AAM due to frictional dissipation is less dominant than radial advection of AAM. Clearly, this process cannot explain the much smaller R17 in MF–0.5 and MF–0.1 than in CTL, suggesting the frictional dissipation is nonnegligible at large radii. To illustrate the impact of boundary layer frictional dissipation, Fig. 10 compares the azimuthal-mean tangential wind averaged over t = 80–100 h between CTL and other experiments using the second MF tapering approach under SST = 29°C. Figure 10 shows that while tangential winds in the 2–4-km layer are less affected, the tangential wind profile in the boundary layer (<1 km) can be considerably affected, with substantially increased vertical wind shear in MF–0.5 and MF–0.1 (marked by the black arrow in Figs. 10a,b), which accounts for the smaller R17 in MF–0.5 and MF–0.1 compared to CTL. This amplified boundary layer vertical wind shear in MF–0.5 and MF–0.1 is attributable to the reduced vertical turbulent mixing of momentum as M_u is turned off therein. With the effective zone of MF tapering being confined with the inner core in

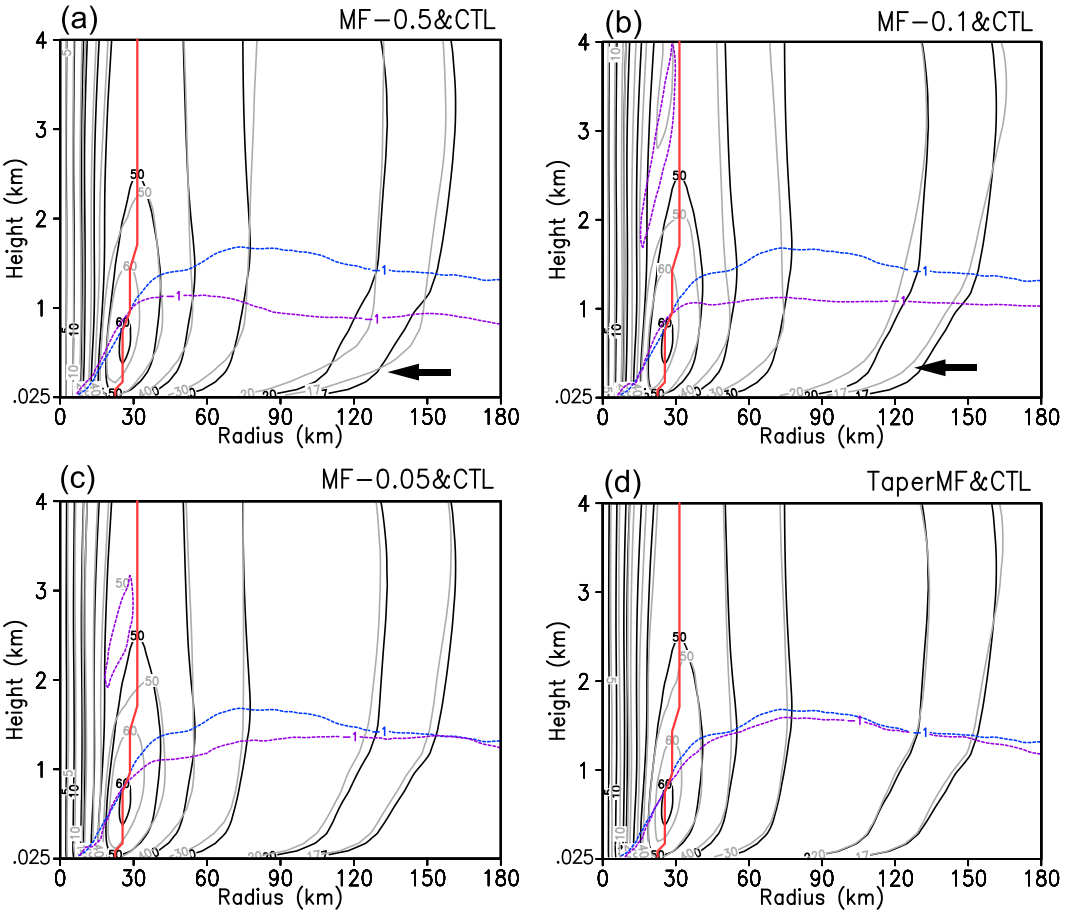

FIG. 10. Radial–height plot of azimuthal-mean tangential wind (contoured at 17, 20, 30, 40, 50, and 60 m s^{-1}) averaged over t = 80–100 h for CTL (black) and other experiments (gray) with SST = 29°C, showing (a) MF–0.5, (b) MF–0.1, (c) MF–0.05, and (d) TaperMF, respectively. In each panel, the blue and purple dashed lines denote $V_r = -1$ m s^{-1} for CTL and the other comparison experiment, respectively. The red line denotes the RMW in CTL and the black arrow marks the location of the contour of 17 m s^{-1}.

MF–0.05 and TaperMF, the shape of boundary layer tangential wind profiles near R17 in these two experiments is nearly identical to that in CTL (Figs. 10c,d).

To understand the faster growth of R17 in CTL than in MF–0.5 and MF–0.1 (Fig. 7c), as discussed earlier, we compared the Hovmöller diagram of azimuthal-mean tangential wind V_T at z = 10 m and radar reflectivity at z = 1 km for CTL and MF–0.5 under SST = 29°C (Fig. 11). A striking difference between Figs. 11a and 11b is that the diurnal cycle of outward and inward propagation of outer rainbands seen in CTL (also seen in TaperMF and MF–0.05, not shown) is difficult to discern in MF–0.5 after t = 100 h. The lack of outer rainband activity in the annulus of r = 90–180 km after t = 100 h is well indicated by purple shading within the blue box in Fig. 11c. Additionally, the 10-m V_T radially outward of the RMW of the CTL TC and inward of r = 120 km is generally ~2 m s^{-1} weaker in MF–0.5 than in CTL (see contours in Fig. 11c), indicating a faster radial decay of tangential wind outside of the RMW in MF–0.5. It should be noted that turning off surface-based MF in the outer region (roughly $r > 3 \times$ RMW; see Fig. 6d) in MF–0.5 also reduces the vertical mixing of water vapor into the upper boundary layer (as suggested by Figs. 5e,f), which explains the weaker rainband activity therein. The reduced diabatic heating and the resulting weakened radial inflow in the outer-core region reduce the inward advection of large AAM, which in part accounts for the much slower growth of R17 with time in MF–0.5 than in CTL. One additional, indirect impact of the weakened outer rainband activity on reducing R17 is through cloud–longwave-radiative forcing, mostly active above the PBL, as reported by Bu et al. (2014).

5. Conclusions

A modified TKE-based eddy-diffusivity mass-flux (EDMF) PBL scheme (hereafter EDMF-TKE) was recently developed by Chen et al. (2022) and then implemented into NOAA's next-generation hurricane forecast model, i.e., Hurricane Analysis and Forecast System (HAFS). This modified scheme reduces the excessive vertical turbulent mixing in high-wind conditions indicated by the original EDMF-TKE and contributes to the improvement

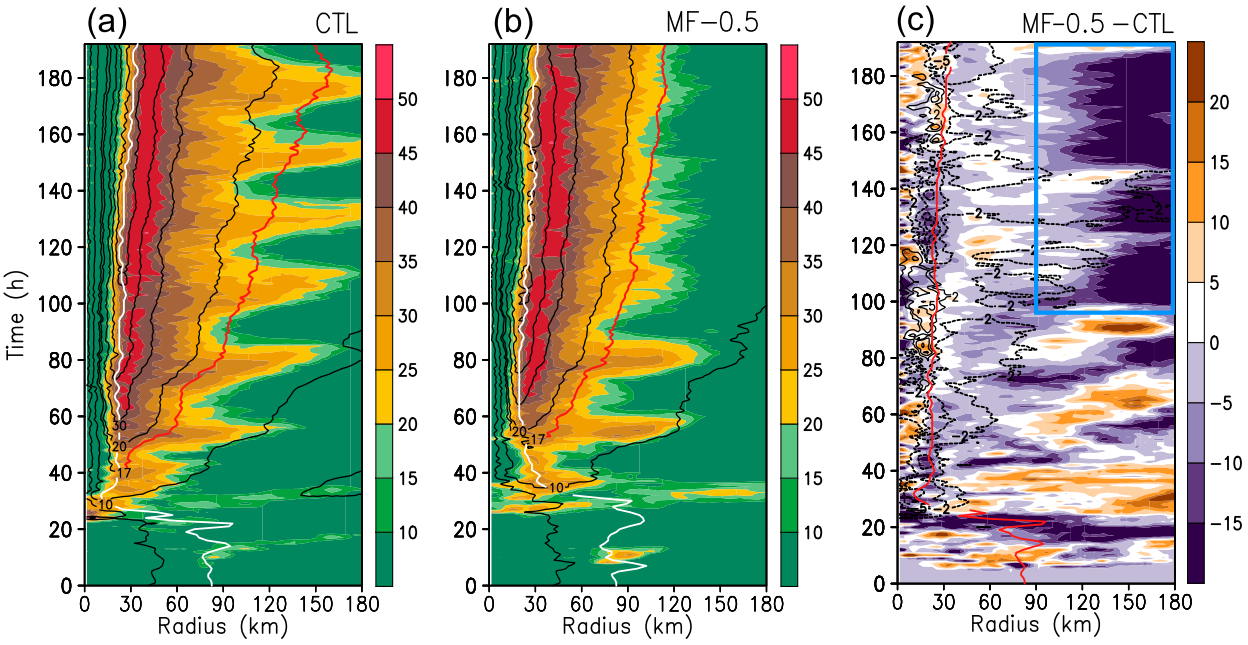

FIG. 11. Hovmöller diagram of azimuthal-mean tangential wind V_T (contoured at 5, 10, 17, 20, 30, 40, 50 m s^{-1}) at z = 10 m and radar reflectivity (dBZ; shading) at z = 1 km from (a) CTL and (b) MF–0.5 experiments under SST = 29°C. (c) Their differences (MF–0.5 − CTL), with differences in radar reflectivity shaded and differences in V_T contoured at −15, −10, −5, −2, 2, 5, and 10 m s^{-1} (negative values are dashed). The red contour in (a) and (b) denotes V_T = 17 m s^{-1}. The white line in (a) and (b) denotes the RMW. The red line in (c) is the RMW from CTL. The blue box in (c) highlights the area lacking in active outer rainbands in MF–0.5.

of HAFS's forecast skill in both tropical cyclone (TC) intensity and structure (Chen et al. 2023). Based upon this modified EDMF-TKE scheme, this study assesses the importance and uncertainty of surface-driven and stratocumulus-top-driven MF components in TC simulations by performing idealized CM1 simulations. Results demonstrate the dominant role of surface-driven MF in the boundary layer turbulent mixing in the mid–upper portion of TC boundary layers outside the radius of maximum wind (RMW). Compared to the simulations using the modified EDMF-TKE scheme with both MF components turned on, simulations excluding surface-driven MF have significantly lower inflow layer depth and stronger inflow outside the RMW, leading to stronger simulated TC intensity and smaller RMW and radius of gale-force wind (R17).

To represent the impact of vertical wind shear on distorting and/or damping rising plumes, this study proposes and tests a new, stratification-based approach of MF tapering by retaining surface-driven MF component only in non-shear-driven boundary layers based on the surface stability parameter ζ, and compares its performance to a wind speed–based approach that tapers off surface-driven MF based on 10-m wind speeds. The main findings are summarized below:

1) The zone where MF tapering occurs (i.e., the effective zone) using the stratification-based approach is dependent on what threshold of ζ is chosen to taper/disable MF, which affects the annulus of enhanced boundary layer inflow. Results show that more-negative thresholds of ζ lead to larger effective zones, which leads to larger annuli of enhanced boundary layer inflow.
2) Both approaches of MF tapering can lead to stronger and more compact inner-core circulations under various sea surface temperatures.
3) R17 is nearly unaffected using the wind speed–based approach of MF tapering. In contrast, R17 is notably reduced by turning off surface-driven MF where $\zeta > -0.1$ or $\zeta > -0.5$, which is in part attributable to the enhanced boundary layer frictional dissipation in the outer-core region.
4) While the wind speed–based approach of MF tapering exerts a marginal impact on inflow layer depth, the stratification-based approach of MF tapering can significantly reduce the inflow layer depth. Among these experiments, the modeled inflow layer depth within 1–4 × RMW is most comparable to the in-situ dropsonde composite of hurricanes by turning off surface-driven MF where $\zeta > -0.05$.

Both approaches of MF tapering under high-wind conditions exert an impact on the TC boundary layer structure, intensity, and structure. The wind speed–based approach of MF tapering defines high-wind or shear-driven boundary layers solely based on 10-m wind speeds ($V_{10} > 20$ m s^{-1}), and it mostly takes effect within the inner-core region when the TC circulation gains sufficient strength. Instead, the stratification-based approach of MF tapering separates shear-driven and buoyancy-driven boundary layers based on ζ, as high-wind, TC boundary layers are nearly neutral (Foster 2013; Chen et al. 2021a; Chen 2022). Given that the stratification-based approach considers both shear and buoyancy effects, it is physically more appealing than the wind speed–based approach. The effective zone of MF tapering using the stratification-based approach shows a more

notable diurnal oscillation in response to the diurnally varying surface buoyancy forcing.

While results in this study suggest $\zeta = -0.05$ may be a reasonable threshold to separate shear-driven and buoyancy-driven boundary layers, we realize that a precise threshold of ζ needs to be determined with more in situ measurements (i.e., surface heat fluxes and frictional velocity) collected in the future, likely through paired observations of dropsondes and small unmanned aircraft systems (Cione et al. 2020), and with a systematic evaluation from operational models (e.g., HAFS) forecasts that can produce realistic TC boundary layer structures against observations (Hazelton et al. 2021; Chen et al. 2023). A recent observational study led by Stopa et al. (2022) shows that a bulk Richardson number (Rib) of −0.012 can effectively separate unstable, and nearly neutral stratification for the marine surface-layer atmosphere (i.e., 0–10-m heights). Given the relationship of $\zeta_{10} \sim 10\text{Rib}$ (Grachev and Fairall 1997; Stopa et al. 2022),[5] one can derive an approximate threshold $\zeta_{10} = -0.12$. Nevertheless, one caveat is that ζ used in this study depends on the height of the bottom model level (i.e., 50 m), and thereby one cannot directly compare the values of ζ and ζ_{10}. To address this issue, we plan to explore a new boundary layer stability parameter that uses the diagnosed boundary layer height (Moeng and Sullivan 1994) rather than the height of the bottom model level; in that way, the threshold of ζ is independent of the configuration of model levels and can yield more insightful results for the future development of PBL parameterizations in high-wind conditions. Last, we note that the proposed modifications to the PBL parameterizations in this study are primarily for TC applications (e.g., HAFS), and rigorous tests are required before considering broader applications in global models.

Acknowledgments. We would like to acknowledge high-performance computing support from Cheyenne (DOI: 10.5065/D6RX99HX) provided by NCAR's Computational and Information Systems Laboratory, sponsored by the National Science Foundation. The authors are grateful for the constructive suggestions from Dr. George Bryan during the early stage of this work. The authors also would like to appreciate the insightful comments from Drs. Kyle Ahern and Andy Hazelton, and three anonymous reviewers that help strengthen the quality of the analysis. Last, we thank Dr. Jun Zhang for kindly providing the observational data for the model verification. This work is supported by the National Oceanic and Atmospheric Administration Grants NA23OAR4590380 and NA21OAR4320190.

Data availability statement. The experiments using the CM1 model are available on NCAR's Cheyenne supercomputer, or by request to Xiaomin Chen (xc0011@uah.edu).

REFERENCES

Ahern, K., R. E. Hart, and M. A. Bourassa, 2021: Asymmetric hurricane boundary layer structure during storm decay. Part I: Formation of descending inflow. *Mon. Wea. Rev.*, **149**, 3851–3874, https://doi.org/10.1175/MWR-D-21-0030.1.

Braun, S. A., and W.-K. Tao, 2000: Sensitivity of high-resolution simulations of Hurricane Bob (1991) to planetary boundary layer parameterizations. *Mon. Wea. Rev.*, **128**, 3941–3961, https://doi.org/10.1175/1520-0493(2000)129%3C3941:SOHRSO%3E2.0.CO;2.

Bryan, G. H., 2012: Effects of surface exchange coefficients and turbulence length scales on the intensity and structure of numerically simulated hurricanes. *Mon. Wea. Rev.*, **140**, 1125–1143, https://doi.org/10.1175/MWR-D-11-00231.1.

——, and J. M. Fritsch, 2002: A benchmark simulation for moist nonhydrostatic numerical models. *Mon. Wea. Rev.*, **130**, 2917–2928, https://doi.org/10.1175/1520-0493(2002)130<2917:ABSFMN>2.0.CO;2.

Bu, Y. P., R. G. Fovell, and K. L. Corbosiero, 2014: Influence of cloud–radiative forcing on tropical cyclone structure. *J. Atmos. Sci.*, **71**, 1644–1662, https://doi.org/10.1175/JAS-D-13-0265.1.

Cangialosi, J. P., E. Blake, M. DeMaria, A. Penny, A. Latto, E. Rappaport, and V. Tallapragada, 2020: Recent progress in tropical cyclone intensity forecasting at the National Hurricane Center. *Wea. Forecasting*, **35**, 1913–1922, https://doi.org/10.1175/WAF-D-20-0059.1.

Chen, X., 2022: How do planetary boundary layer schemes perform in hurricane conditions: A comparison with large-eddy simulations. *J. Adv. Model. Earth Syst.*, **14**, e2022MS003088, https://doi.org/10.1029/2022MS003088.

——, and G. H. Bryan, 2021: Role of advection of parameterized turbulence kinetic energy in idealized tropical cyclone simulations. *J. Atmos. Sci.*, **78**, 3559–3574, https://doi.org/10.1175/JAS-D-21-0088.1.

——, ——, J. A. Zhang, J. J. Cione, and F. D. Marks, 2021a: A framework for simulating the tropical cyclone boundary layer using large-eddy simulation and its use in evaluating PBL parameterizations. *J. Atmos. Sci.*, **78**, 3593–3611, https://doi.org/10.1175/JAS-D-20-0227.1.

——, M. Xue, B. Zhou, J. Fang, J. A. Zhang, and F. D. Marks, 2021b: Effect of scale-aware planetary boundary layer schemes on tropical cyclone intensification and structural changes in the gray zone. *Mon. Wea. Rev.*, **149**, 2079–2095, https://doi.org/10.1175/MWR-D-20-0297.1.

——, G. H. Bryan, A. Hazelton, F. D. Marks, and P. Fitzpatrick, 2022: Evaluation and improvement of a TKE-based eddy-diffusivity mass-flux (EDMF) planetary boundary layer scheme in hurricane conditions. *Wea. Forecasting*, **37**, 935–951, https://doi.org/10.1175/WAF-D-21-0168.1.

——, A. Hazelton, F. D. Marks, G. J. Alaka Jr., and C. Zhang, 2023: Performance of an improved TKE-based eddy-diffusivity mass-flux (EDMF) PBL scheme in 2021 hurricane forecasts from Hurricane Analysis And Forecast System. *Wea. Forecasting*, **38**, 321–336, https://doi.org/10.1175/WAF-D-22-0140.1.

Cione, J. J., and Coauthors, 2020: Eye of the storm: Observing hurricanes with a small unmanned aircraft system. *Bull. Amer. Meteor. Soc.*, **101**, E186–E205, https://doi.org/10.1175/BAMS-D-19-0169.1.

Dunion, J. P., 2011: Rewriting the climatology of the tropical North Atlantic and Caribbean Sea atmosphere. *J. Climate*, **24**, 893–908, https://doi.org/10.1175/2010JCLI3496.1.

Fischer, M. S., B. H. Tang, and K. L. Corbosiero, 2019: A climatological analysis of tropical cyclone rapid intensification in environments of upper-tropospheric troughs. *Mon. Wea. Rev.*, **147**, 3693–3719, https://doi.org/10.1175/MWR-D-19-0013.1.

[5] $\zeta_{10} = z_{10}\,\mathrm{L}^{-1}$, where $z_{10} = 10$ m.

Foster, R., 2013: Signature of large aspect ratio roll vortices in synthetic aperture radar images of tropical cyclones. *Oceanography*, **26** (2), 58–67, https://doi.org/10.5670/oceanog.2013.31.

Grachev, A. A., and C. W. Fairall, 1997: Dependence of the Monin–Obukhov stability parameter on the bulk Richardson number over the ocean. *J. Appl. Meteor.*, **36**, 406–414, https://doi.org/10.1175/1520-0450(1997)036<0406:DOTMOS>2.0.CO;2.

Gu, J.-F., Z.-M. Tan, and X. Qiu, 2016: Quadrant-dependent evolution of low-level tangential wind of a tropical cyclone in the shear flow. *J. Atmos. Sci.*, **73**, 1159–1177, https://doi.org/10.1175/JAS-D-15-0165.1.

Han, J., and C. S. Bretherton, 2019: TKE-based moist eddy-diffusivity mass-flux (EDMF) parameterization for vertical turbulent mixing. *Wea. Forecasting*, **34**, 869–886, https://doi.org/10.1175/WAF-D-18-0146.1.

——, M. L. Witek, J. Teixeira, R. Sun, H.-L. Pan, J. K. Fletcher, and C. S. Bretherton, 2016: Implementation in the NCEP GFS of a hybrid eddy-diffusivity mass-flux (EDMF) boundary layer parameterization with dissipative heating and modified stable boundary layer mixing. *Wea. Forecasting*, **31**, 341–352, https://doi.org/10.1175/WAF-D-15-0053.1.

Hazelton, A., and Coauthors, 2021: 2019 Atlantic hurricane forecasts from the global-nested Hurricane Analysis and Forecast System: Composite statistics and key events. *Wea. Forecasting*, **36**, 519–538, https://doi.org/10.1175/WAF-D-20-0044.1.

Hill, K. A., and G. M. Lackmann, 2009: Analysis of idealized tropical cyclone simulations using the Weather Research and Forecasting Model: Sensitivity to turbulence parameterization and grid spacing. *Mon. Wea. Rev.*, **137**, 745–765, https://doi.org/10.1175/2008MWR2220.1.

Moeng, C.-H., and P. P. Sullivan, 1994: A comparison of shear- and buoyancy-driven planetary boundary layer flows. *J. Atmos. Sci.*, **51**, 999–1022, https://doi.org/10.1175/1520-0469(1994)051<0999:ACOSAB>2.0.CO;2.

Nolan, D. S., J. A. Zhang, and D. P. Stern, 2009: Evaluation of planetary boundary layer parameterizations in tropical cyclones by comparison of in situ observations and high-resolution simulations of Hurricane Isabel (2003). Part I: Initialization, maximum winds, and the outer-core boundary layer. *Mon. Wea. Rev.*, **137**, 3651–3674, https://doi.org/10.1175/2009MWR2785.1.

Olson, J. B., J. S. Kenyon, W. A. Angevine, J. M. Brown, M. Pagowski, and K. Sušelj, 2019: A description of the MYNN-EDMF scheme and the coupling to other components in WRF–ARW. NOAA Tech. Memo. OAR GSD 61, 42 pp., https://repository.library.noaa.gov/view/noaa/19837.

Siebesma, A. P., and J. Teixeira, 2000: An advection-diffusion scheme for the convective boundary layer: Description and 1D-results. *Proc. 14th Symp. on Boundary Layers and Turbulence*, Aspen, CO, Amer. Meteor. Soc., 4.16, https://ams.confex.com/ams/AugAspen/techprogram/paper_14840.htm.

Smith, R. K., and G. L. Thomsen, 2010: Dependence of tropical-cyclone intensification on the boundary-layer representation in a numerical model. *Quart. J. Roy. Meteor. Soc.*, **136**, 1671–1685, https://doi.org/10.1002/qj.687.

——, and M. T. Montgomery, 2015: Toward clarity on understanding tropical cyclone intensification. *J. Atmos. Sci.*, **72**, 3020–3031, https://doi.org/10.1175/JAS-D-15-0017.1.

Soares, P. M. M., P. M. A. Miranda, A. P. Siebesma, and J. Teixeira, 2004: An eddy-diffusivity/mass-flux parametrization for dry and shallow cumulus convection. *Quart. J. Roy. Meteor. Soc.*, **130**, 3365–3383, https://doi.org/10.1256/qj.03.223.

Stopa, J. E., C. Wang, D. Vandemark, R. Foster, A. Mouche, and B. Chapron, 2022: Automated global classification of surface layer stratification using high-resolution sea surface roughness measurements by satellite synthetic aperture radar. *Geophys. Res. Lett.*, **49**, e2022GL098686, https://doi.org/10.1029/2022GL098686.

Zhang, J. A., and E. W. Uhlhorn, 2012: Hurricane sea surface inflow angle and an observation-based parametric model. *Mon. Wea. Rev.*, **140**, 3587–3605, https://doi.org/10.1175/MWR-D-11-00339.1.

——, R. F. Rogers, D. S. Nolan, and F. D. Marks, 2011: On the characteristic height scales of the hurricane boundary layer. *Mon. Wea. Rev.*, **139**, 2523–2535, https://doi.org/10.1175/MWR-D-10-05017.1.

——, D. S. Nolan, R. F. Rogers, and V. Tallapragada, 2015: Evaluating the impact of improvements in the boundary layer parameterization on hurricane intensity and structure forecasts in HWRF. *Mon. Wea. Rev.*, **143**, 3136–3155, https://doi.org/10.1175/MWR-D-14-00339.1.